

1 **The role of pre-existing discontinuities in the development of**  
2 **extensional faults: an analog modeling perspective**

3  
4 Lorenzo Bonini<sup>1,3\*</sup>, Roberto Basili<sup>2</sup>, Giovanni Toscani<sup>3</sup>, Pierfrancesco Burrato<sup>2</sup>, Silvio Seno<sup>3</sup>,  
5 Gianluca Valensise<sup>2</sup>

6 <sup>1</sup> *Dipartimento di Matematica e Geoscienze, Università di Trieste, Trieste, ITALY*

7 <sup>2</sup> *Istituto Nazionale di Geofisica e Vulcanologia, Rome, ITALY*

8 <sup>3</sup> *Dipartimento di Scienze della Terra e dell'Ambiente, Università di Pavia, ITALY*

9 \*Corresponding author: Lorenzo Bonini, e-mail address: lbonini@units.it

10

11

12 **Abstract**

13 Several mountainous regions are currently affected by syn- or post-orogenic active extension. We investigate  
14 how a newly-formed normal fault interacts with structures inherited from a previous contractional phase. To  
15 this end, we use analog models that adopt an innovative technique for performing a precut that mimics such  
16 inherited structures into a clay layer; this clay layer is laid on top of a master fault simulated by two rigid  
17 blocks sliding along an inclined plane. We carry out six experiments with variously oriented precuts and  
18 compare the results with those obtained in a reference isotropic experiment. All other conditions are identical  
19 for all seven realizations. Fault evolution is monitored by taking closely-spaced snapshots analyzed through  
20 the Digital Image Correlation method. We find that the upward propagation of the normal fault can be either  
21 accelerated or decelerated depending on the presence of a precut and its orientation. Such precuts can also  
22 promote or inhibit the formation of bending-moment faults. These interactions between master fault and precut  
23 also affect the shape of the fault-related syncline-anticline pair.

24

25 **Keywords.** Extension, Normal fault, Pre-existing fault, Analogue modeling, Accommodation space, Blind  
26 fault, Active tectonics

27

28

## 29        **1. Introduction**

30 Long-term geological processes, such as the growth and development of extensional faults from their  
31 embryonic stage (blind faults) to a mature stage (basin-bounding faults), cannot be appreciated on a human  
32 timescale. Two fundamental options exist to overcome this limitation. One is the analysis of natural faults at  
33 different stages of maturity at different locations; the other is the analysis of faults through modeling. In  
34 principle, the first strategy should be preferred, but identifying a suite of faults having different age and sharing  
35 a similar tectonic framework may turn out to be extremely difficult. The second strategy is easier to pursue but  
36 its assumptions and limitations need to be carefully considered. Conceptual evolutionary models predict that  
37 in a uniform material faults form through the coalescence of Mode I fractures subsequently reactivated in shear  
38 (e.g. Segall and Pollard, 1983; Martel et al., 1988; Pollard and Aydin, 1988; Mandl, 2000; Scholz, 2002;  
39 Gudmundsson; 2011). The growth history of a natural extensional fault, however, is often more complex than  
40 one might expect from such simple models. Rock variability and the presence of older structures (e.g., pre-  
41 existing faults) may play a crucial role, for instance, in affecting the geometry of the fault and its extent. These  
42 occurrences are nearly inevitable when extension takes place in mountain belts where syn- or post-orogenic  
43 extensional structures develop in complex settings created by the superposition of different rock types  
44 separated by thrust faults (Fig. 1). Several major mountain belts are currently undergoing extension, including  
45 the Himalayas (Molnar et al., 1993), the Andes (Dalmayrac, and Molnar, 1981), the Basin and Range  
46 (Wernicke, 1981; Malavieille, 1993), the Taiwan Orogen (Teng, 1996), the Alps (Selverstone, 1988; Bonini  
47 et al., 2010; Maino et al., 2013), the Apennines (Elter et al., 1975; Hyppolite et al., 1994; Tavarnelli et al.,  
48 2001; Tavarnelli et al., 2003), and the Pyrenees (Chevrot et al., 2011; Lucan and Ortuño, 2012). The growth  
49 of faults in these heterogeneous layered settings has been the object of a number of studies (see van Gent et  
50 al., 2010; Roche et al., 2013 and references therein). A few studies have also discussed how faults develop  
51 when interacting with pre-existing mechanical weaknesses, such as inherited fault zones or thin weak rock  
52 layers (e.g., Williams et al., 1989; Faccenna et al., 1995; Tavarnelli et al., 1996a; Tavarnelli et al., 1996b;  
53 Cosgrove and Ameen, 2000; Withjack and Callaway, 2000; Tavarnelli et al., 2001; Tvedt et al., 2013; Di  
54 Domenica et al., 2014; Tong et al., 2014). In addition, theoretical and numerical analyses have shown that even  
55 thin mechanical weaknesses may deflect, stop, decelerate or accelerate the propagation of new faults (e.g.,  
56 Cooke and Pollard, 1997; Roering et al., 1997; Mandl, 2000).

57 In this study we investigate how the growth of an extensional fault is affected by the presence of a pre-existing  
58 frictional discontinuity located in the rock volume overlying the fault itself. To this end we performed analog  
59 modeling through a series of six experiments using a clay layer; in each realization a pre-cut is placed with  
60 variable orientation with respect to a master fault, thus simulating simple but different inherited structural  
61 settings. The results of these experiments are compared with the state of deformation of a reference isotropic  
62 experiment (no pre-cut above the fault). We quantify the strain-rate distribution inside the different experiments  
63 and reconstruct the evolution of any fault-related folds at significant steps.

64 Our results indicate that during the evolution of a growing extensional fault any pre-existing discontinuity  
65 affects (i) the propagation rate of new faults and their ability to reach the surface, (ii) the development of  
66 secondary brittle structures related to fault-propagation folding, and (iii) the shape of the related  
67 accommodation space together with the migration of the syncline hinge through time. We claim that these  
68 elements can be related to the presence and orientation of pre-existing mechanical discontinuities in natural  
69 cases.

70

## 71 **2. Method and experimental setup**

72 Two analog materials are commonly used to investigate the evolution of extensional structures: dry sand and  
73 wet clay. These two materials have different properties and are selected by modelers based on the goal to be  
74 pursued (Eisenstadt and Sims, 2005). Dry sand is classically used to analyze broad deformation zones and fault  
75 kinematics (e.g. Davis et al., 1983; McClay and Bonora, 2001; Ahmad et al., 2014; Toscani et al., 2014;  
76 Philippon et al., 2015), as well as the brittle surface expression of blind faults (e.g. Bonini et al., 2011; Galuppo  
77 et al., 2015). Wet clay is especially used in studies devoted to analyzing the development of faults and fractures  
78 (e.g. Cloos, 1929; Withjack and Jamison, 1986), and the potential reactivation of pre-existing faults (e.g.  
79 Eisenstadt and Sims, 2005; Bonini et al., 2014).

80 In this study we use wet clay to simulate the deformation patterns associated with an extensional, initially  
81 blind, master fault (Fig. 2). As regards the clay type, we adopt wet kaolin because it is one of the most used  
82 and tested clay types for simulating faulting and folding in brittle crustal rocks (e.g., Withjack et al., 1990;  
83 Eisenstadt and Sims, 2005; Miller and Mitra, 2011; Cooke and van der Elst, 2012).

84 The experimental apparatus is composed by two rigid blocks juxtaposed along  $45^\circ$  sloping sides, which  
85 represent the plane of the master fault. We adopted a dip of  $45^\circ$  for the master fault because worldwide  
86 compilations of normal faults show that this is the most common value in tectonically active regions (Jackson  
87 and Withe, 1989; Collettini and Sibson, 2001).

88 Wet clay covers the two rigid blocks and represents rocks located above the master fault (Fig. 2). The footwall  
89 block is fixed, whereas the hanging wall block is allowed to slide downward along the sloping side. The  
90 displacement of the moving block is controlled by a stepper-motor at a constant velocity of 0.005 mm/s. The  
91 clay is wet kaolin with density of  $1.65 \text{ g/cm}^3$ , water content of 60% by mass, shear strength in the range 50-  
92 120 Pa (Eisenstadt and Sims, 2005; Cooke and van der Elst, 2012), and friction coefficient equal to 0.6. Using  
93 well established scaling rules (e.g., Hubbert, 1937) we assume that under these experimental conditions 1 cm  
94 in our experiment corresponds to about 1 km in nature. In all the experiments the clay layer is 5 cm-thick, thus  
95 representing a 5 km-thick brittle continental crust in nature. Black quartz sand grains are placed on the model  
96 side to act as displacement markers by creating a visual contrast with the pale-colored clay, hence allowing the  
97 model evolution to be monitored. In addition to mapping brittle structural features such as newly-formed  
98 fractures and faults, this technique allows us to identify peculiar features of the displacement field, including  
99 the trishear zone (Hardy and Ford, 1997; Allmendinger, 1998), and to obtain a high-resolution quantification  
100 of the deformation taking place during the experiments. Fault evolution, displacement field, and strain-rate  
101 distribution are investigated through the Digital Image Correlation method (D.I.C.; Pan et al., 2009) by  
102 analyzing side photographs taken at every 0.5 mm of displacement on the master fault using the PIVlab  
103 software (Garcia, 2011; Thielicke, 2014; Thielicke and Stamhuis, 2014).

104 What makes wet kaolin especially suitable for our purposes is the possibility of precutting the clay layer to  
105 introduce thin mechanical discontinuities that simulate pre-existing faults or thin layers of weaker rocks. The  
106 precut is  $\sim 200 \mu\text{m}$  thick and is obtained by sliding an electrified blade into the clay layer before starting the  
107 deformation process. This technique has already been applied to reproduce long-lived faults both in strike-slip  
108 systems (Cooke et al. 2013) and in extensional regimes (Paul and Mitra, 2013; Bonini et al., 2014).

109 Using this setup we conduct seven experiments named from E1 through E7 (Fig. 2a-h, Table 1). E1 is a  
110 mechanically isotropic experiment (i.e. without precut). E2 has a horizontal precut in the middle of the clay  
111 layer. E3, E4 and E5 have precuts dipping  $10^\circ$ ,  $30^\circ$ , and  $45^\circ$ , respectively, with the same dip direction of the

112 master fault (i.e., synthetic planes). The last two experiments, E6 and E7, have a precut dipping  $45^\circ$  and  $30^\circ$ ,  
113 respectively, both with opposite dip direction with respect to the master fault (i.e. antithetic planes).

114 The precut is spatially arranged such that it consistently runs 2.5 cm above the tip of the master fault for all  
115 experiments. For simplicity, we show snapshots taken at the end of regular intervals of 0.5 cm of displacement  
116 on the master fault. In the following, each interval is denoted as follows: 0.0-0.5 cm, Early Stage; 0.5-1.0 cm,  
117 Middle Stage; 1.0-1.5 cm, Late Stage. For each stage we provide a display of fault and fracture traces, a set of  
118 displacement vectors, and the strain-rate distribution within the clay layer.

119

### 120 **3. Experimental results**

#### 121 **3.1. Experiment E1: isotropic**

122 During the Early Stage a newly-formed synthetic fault and a smaller antithetic fault propagate upward from  
123 the upper tip of the master fault (Fig. 3a), and the fault-propagation folding produces a gentle monocline. The  
124 displacement field indicates a trishear zone located above the tip of the master fault (Fig. 3b), and the strain  
125 analysis shows that most of the deformation is related to the upward-propagating synthetic fault (Fig. 3c).

126 In the Middle Stage the first synthetic fault slightly propagates upward (Fig. 3d) and two branches appear on  
127 both sides of it. Such faults grow by connecting previously-formed small cracks. At the free surface, the  
128 steepening of the monocline produces two downward-propagating faults (bending-moment faults).

129 During the Late Stage upward- and downward-propagating faults connect to each other, thereby forming a  
130 continuous fault plane that extends from the tip of the rigid hanging wall block up to the free surface (Fig. 3g),  
131 and there it forms a fault free face. Displacement vectors confirm the decoupling between the two sides of the  
132 fault in the clay layer, showing no motion of the footwall (Fig. 3h). Overall the strain-rate distribution shows  
133 that most of the deformation is concentrated along the main synthetic fault, though a secondary synthetic  
134 structure located in its hanging wall displays significant activity (Fig. 3i). The heterogeneous strain-rate  
135 distribution along the fault traces suggests that these faults form by linking small cracks.

136 In summary, the isotropic model shows that after about 1.5 cm of displacement imparted to the rigid blocks  
137 the fault has propagated enough to reach the free surface. This value is then used as a reference maximum  
138 displacement to compare the results obtained from the other experiments at the same step. In case the  
139 propagating fault reaches the surface before this reference maximum displacement, the experiment is stopped.

### 140 **3.2. Experiment E2: horizontal precut**

141 In the Early Stage a newly-formed, synthetic fault propagates upward and intersects the horizontal precut (Fig.  
142 4); a small fracture is located above its upper tip, and a bending-moment fault at the free surface accommodates  
143 the development of the monocline (Fig. 4a). Displacement vectors depict a trishear zone whose apical angle is  
144 located close to the precut (Fig. 4b), attesting faster upward fault propagation than in E1 (compare with Fig.  
145 3b). The strain-rate distribution shows that most of the deformation is confined below the precut (Fig. 4c).  
146 As the experiment proceeds to the Middle Stage the upward-propagating fault crosses the precut and connects  
147 with overlying fractures and with a newly-formed downward-propagating fault. This new fault system cuts the  
148 entire clay layer, as testified by the absence of displacement in its footwall (Fig. 4d). The experiment is thus  
149 stopped at the end of this stage. The fault-related folding at this stage produces bending-moment faults at the  
150 free surface. The strain-rate distribution shows that most of the slip falls along fault segments that formed in  
151 the Early Stage (Fig. 4e).

### 152 **3.3. Experiment E3: synthetic, 10° dipping precut**

153 During the Early Stage a new fault forms and propagates upward at a slower rate than that of E2, yet faster  
154 than the homologous fault in E1 (Fig. 5a). Unlike the first two experiments, no brittle structures are seen above  
155 the precut. The displacement field shows a trishear zone that crosses the precut (Fig. 5b). The vectors within  
156 the trishear zone exhibit a larger horizontal component than in E1 and E2. The strain analysis shows only  
157 diffuse deformation above the precut (Fig. 5c).

158 In the Middle Stage the upward-propagating fault reaches the discontinuity and stops (Fig. 5d, 5f); only few  
159 secondary fractures form at its tip without significant shearing. Two antithetic faults forms in the hanging wall  
160 of the master fault and a new bending-moments fault accommodates extension at the free surface. The strain  
161 analysis shows that most of the deformation is confined below the precut (Fig. 5f).

162 In the Late Stage the upper tip of the upward-propagating fault remains in the vicinity of the precut (Fig. 5g).  
163 Brittle deformation is accommodated in its footwall by another small fracture located close to the precut and  
164 by bending-moment faults. The strain-rate distribution and displacement vectors show that there is no  
165 connection between upward- and downward-propagating structures. Therefore, at the final step of this  
166 experiment the slip at depth is not transferred all the way to the free surface.

### 167 **3.4. Experiment E4: synthetic, 30° dipping precut**

168 During the Early Stage a new fault forms at tip of the master fault and by propagating upward quickly reaches  
169 the precut (Fig. 6a). Both the displacement field and the strain-rate distribution show that the upper part of the  
170 precut has been slightly reactivated. The composite structure that includes the newly-formed fault and the  
171 reactivated precut inhibits the formation of a trishear zone, leaving the footwall almost undeformed (Figs 6b,  
172 6c). In the Middle Stage a new synthetic fault forms in the footwall of the previously formed fault (Fig. 6d)  
173 and slip on the precut increases (Figs. 6e, 6f). Small fractures form in the zone where newly-formed faults  
174 meet the reactivated section of the precut. These fractures appear to be related to the flexure of the hanging-  
175 wall block due to the sliding along the composite structure. In the Late Stage (Fig. 6g) the displacement vectors  
176 and the strain-rate distribution show that this composite structure reaches a mature stage and the displacement  
177 of the rigid blocks is transferred up to the free surface through the precut (Figs 6h, 6i). A secondary synthetic  
178 fault located in the hanging wall of the composite structure propagates a bit farther upward, yet it does not  
179 reach the free surface. Unlike previous experiments (E1, E2, E3), no bending-moment faults are formed at  
180 the free surface.

### 181 **3.5. Experiment E5: synthetic, 45° dipping precut**

182 In the Early Stage an upward-propagating fault reaches the precut, forming a composite fault that immediately  
183 transfers the displacement all the way to the free surface (Fig. 7). Both the displacement field and strain-rate  
184 distribution (Fig 7b, c) show that slip is rather uniformly distributed along the precut. The experiment is then  
185 stopped.

### 186 **3.6. Experiment E6: antithetic, 45° dipping precut**

187 During the Early Stage a new fault develops from the tip of the master fault (Fig. 8); its propagation produces  
188 a somehow irregular trishear zone above it (Fig. 8b). The strain-rate distribution shows a partial reactivation  
189 of the precut, especially in the section near the newly formed fault (Fig. 8c). In the Middle Stage the upward-  
190 propagating fault reaches the precut and stops (Fig. 8d). Meanwhile, small fractures form in the hanging wall  
191 of the precut, some due to bending. Near the free surface the horizontal component of displacement dominates,  
192 thereby promoting the formation of bending-moment faults that are more evident in this experiment than in all  
193 other experiments (Fig. 8e). The strain-rate distribution shows that much of the deformation is localized on the  
194 surface faults (Fig. 8f). During the Late Stage (Fig. 8g) the upward-propagating fault splits into two splays and  
195 crosses the precut. Bending-moment faults are well-developed and exhibit a sizable vertical displacement; yet

196 they do not show a direct connection with the upward-propagating faults (Fig. 8h). The strain-rate distribution  
197 shows the reactivation of the precut (Fig. 8i).

### 198 **3.7. Experiment E7: antithetic, 30° dipping precut**

199 In the Early Stage (Fig. 9) the upward-propagating fault is slightly more developed and the displacement field  
200 is less irregular than in E6 (Figs 9b, 8b). The strain-rate distribution shows only a modest reactivation along  
201 the precut and most of the strain is concentrated along newly-formed faults (Fig. 9c). During the Middle Stage  
202 the upward-propagating fault reaches the precut and bending-moment faults start propagating downward from  
203 the free surface (Fig. 9d, e). In this stage the strain-rate distribution shows that the precut is not reactivated and  
204 part of the deformation focuses along an embryonic antithetic fault (Fig. 9f). In the Late Stage upward- and  
205 downward-propagating faults are almost connected (Fig. 9g), as testified by the displacement vectors and by  
206 the strain-rate distribution (Figs 9h, 9i). Similarly to E6, also in this experiment bending-moment faults exhibit  
207 a considerable vertical offset, but in this case also the newly-formed antithetic fault produces significant offset  
208 of the free surface.

209

## 210 **4. Discussion**

211 In all experiments with precuts (E2-7), and starting from the very early development stage, the geometry and  
212 kinematics of brittle structures, the shape of the related folds, the displacement fields, and the strain-rate  
213 distributions differ from those seen following the isotropic experiment (E1). These differences are analyzed in  
214 detail in the following sections (see summary of results in Table 1).

### 215 **4.1. Upward propagation of new faults**

216 The role of mechanical discontinuities on the propagation of fractures and faults represents one of the main  
217 problems faced by fracture mechanics and material science (see Gudmundsson, 2011, for a summary); as such,  
218 it has been the object of several studies. Numerical models, and particularly those based on boundary elements  
219 approaches (e.g., Cooke and Pollard, 1997; Roering et al., 1997; Cooke et al., 2000; d'Alessio and Martel,  
220 2004; Cooke and Madden, 2014), yielded encouraging results for geological applications. Among other  
221 workers, Roering et al. (1997) analyzed the influence of horizontal, bedding-plane slip on the propagation of  
222 a newly-formed, blind reverse fault, suggesting: 1) an increased tendency of the new fault to propagate upward

223 when the frictional plane is above it, and 2) a reduced tendency for the same new fault to propagate further  
224 when its tip reaches the pre-existing plane.

225 Although we investigate how pre-existing discontinuities affect the evolution of a normal fault, our  
226 experiments yield results qualitatively similar to those obtained by Roering et al. (1997); we observe different  
227 velocities in fault propagation, however, also depending on 1) the location of the upward-propagating fault  
228 and 2) the orientation of the pre-existing discontinuities (precuts). The upward propagation rate of our newly-  
229 formed faults is not constant over time (Fig. 10a), but it either accelerates or decelerates during all experiments.  
230 Below we first recall how these faults grow in the isotropic experiment, then analyze the fault-propagation rate  
231 in experiments with differently oriented precut.

#### 232 *4.1.1. The isotropic model*

233 The main fractures that can be visually detected on the side of the clay layer in the Early Stage of the isotropic  
234 experiment (E1) formed with an acute angle with the vertical  $\sigma_1$  (ca.  $30^\circ$ ), the characteristic angle of shear  
235 fractures (Fig. 3a). Such shear fractures (Mode II) - i.e. the upward-propagating faults - connect to each other  
236 through small vertical fractures reminiscent of wing cracks (Mode I). In general, this propagation pattern is  
237 similar to that expected from crack models and it has been observed both in laboratory tests on rock samples  
238 and in field studies (see Scholz, 2002 for a summary and references on this topic). The profile of upward  
239 propagation of these faults reflects this process (Fig. 10a).

240 At the very beginning of the experiment the stress concentration at the buried tip of the master fault (i.e. at the  
241 boundary between the rigid blocks) increases and generates small *en echelon* Mode I fractures, resulting in a  
242 low fault propagation rate (Fig. 10a). When the small, Mode I fractures connect to one another, and become  
243 visually detectable Mode II fractures, the propagation rate increases abruptly and the shear fractures develop  
244 up to 1.5 cm from the original location of the tip of the master fault. This process is followed by another phase  
245 of Mode I crack formation, and consequently the fault propagation slows down. During the Late Stage the  
246 upward-propagating fault connects through Mode I cracks located at its tip with downward-propagating faults,  
247 thereby increasing the extent of its upward propagation.

248 In summary, the upward propagation rate of newly-formed faults in the isotropic experiment is not constant;  
249 it is very slow during the formation of Mode I cracks, but increases abruptly when the cracks start connecting  
250 and forming shear fractures. This produces an asymmetric propagation profile, with a nucleation phase

251 dominated by the formation of small cracks at the tip of the shear fractures and limited upward propagation,  
252 followed by a growing phase where small cracks connect to one another to form larger shear fractures, thus  
253 determining faster upward propagation.

#### 254 *4.1.2. Fault-tip upward propagation below the precut*

255 At the very beginning of all experiments with precut, the characteristics of the upward propagation of new  
256 faults are rather similar to those seen in the isotropic experiment (Fig. 10b). However, significant differences  
257 in the upward propagation rates start appearing later on, when the newly-formed, upward-propagating shear  
258 fractures extend beyond 1 cm distance from the base of the clay layer. At this point, in experiments where the  
259 precut is antithetic to the master fault the upward-propagation rate of newly-formed faults is slightly faster  
260 than in the isotropic case (Fig. 10b) but slower than in the experiment where the precut is horizontal. The  
261 upward-propagation rate of newly-formed faults becomes increasingly faster for an increase in the dip of the  
262 precut in experiments where the precut is synthetic to the master fault. Our results thus confirm that  
263 discontinuities located above a fault accelerate its upward propagation rate, but this tendency is controlled by  
264 the dip angle and dip direction of the precut. This occurrence is probably related to the stress intensity at the  
265 propagating tip of upward-propagating faults; as shown by the strain analysis in the various experiments, which  
266 is larger when slip on the discontinuity is larger.

#### 267 *4.1.3. Fault-tip upward propagation across the precut*

268 A propagating fracture that meets a discontinuity may stop, be deflected, or penetrate such discontinuity. The  
269 works by Hutchinson (1996), Xu et al. (2003), and Wang and Xu (2006) established that the behavior of the  
270 propagating fracture strongly depends on the *toughness* of the encountered discontinuity, i.e. on the ability of  
271 a material containing a crack to resist fracturing. When the toughness is larger than the total strain energy, the  
272 propagating fracture penetrates the discontinuity. Conversely, when the toughness is lower than the total strain  
273 energy, the propagating fracture is deflected and joins the discontinuity.

274 In our experiments we observe that the precut orientation controls the propagation process of newly-formed  
275 faults when their tip approaches the precut itself. We also observe that a steeper precut dip angle, which  
276 determines an increased shear stress with respect to normal stress, favors slip along the precut. More slip is  
277 thus indicative of a relatively lower toughness of the discontinuity, and consequently it is also indicative of a  
278 promoted fracture deflection. The deflection of upward-propagating faults is promoted in experiments where

279 the dip of the precut is  $> 10^\circ$  (E4, E5, E6, and E7; Fig. 10b). In experiments with antithetic precut, the sense  
280 of slip on the precut is opposite to that of the main, upward-propagating faults; hence, deflection is inhibited  
281 along such an unfavorably oriented plane, resulting in a delayed upward-propagation of newly-formed faults.

#### 282 **4.1.4. Fault-tip upward propagation above the precut**

283 In E4 and E5 the newly-formed faults reactivate the precut and quickly reach the free surface. In E2 the upward-  
284 propagating fault accelerates after connecting with the horizontal precut. In all other experiments (E3, E6, and  
285 E7) the newly-formed faults decelerate their upward propagation as they extend beyond the precut (Fig. 10b).  
286 In these experiments, such deceleration is probably related to the slip on the precut that accommodates part of  
287 the shear strain.

#### 288 **4.2. Antithetic faults**

289 Another important difference between the isotropic experiment (E1) and the experiments with precut (E2-7)  
290 concerns the formation of antithetic faults (Figs. 3-9). In the isotropic case, an antithetic fault evolves  
291 throughout the experiment and accommodates the material deformation in the hanging wall of the main  
292 synthetic upward-propagating faults (Fig. 3). It nucleated at the bend formed by the master fault on the rigid  
293 blocks and the newly-formed upward-propagating fault. The same is seen in E3 (Fig. 5), but in this case the  
294 antithetic faults are located at the bends of the synthetic upward-propagating fault and terminate their own  
295 propagation against the precut.

296 In E2 the antithetic faults cannot be visually detected (left panels in Fig. 4), though some strain concentrates  
297 where an antithetic fault may be expected to form (fig. 4e), i.e. on the hanging wall side of the trishear zone.  
298 Such an occurrence can be explained by the smooth trajectory of the synthetic fault, which derives from the  
299 faster growth rate and lower hanging wall deformation than those seen in other experiments.

300 In E4 and E5 (Figs. 6, 7) the synthetic precuts have a dip  $\geq 30^\circ$  and have been partially (E4) or totally  
301 reactivated (E5). The reactivation prevents the formation of new antithetic faults by accommodating most of  
302 the hanging wall deformation.

303 In E6, the precut is antithetic with respect to both the master fault and the newly-formed upward-propagating  
304 faults. In this case, the partial reactivation of the precut prevents the formation of new antithetic faults (Fig. 8).

305 In E7, the antithetic precut only partially prevents the formation of antithetic structures because its reactivation  
306 occurs only in the very early stage of deformation (Fig. 9a). No antithetic faults are formed in later stages

307 (Figs. 9f, 9i), although a strain concentration is seen along an alignment whose attitude and dip are compatible  
308 with those of an incipient antithetic fault plane.

### 309 **4.3. Shallow brittle structures**

310 During all experiments, the movement of the rigid blocks and the development of upward-propagating faults  
311 produce folding, that is to say, bending of the free surface: anticlines above the tip of the master fault and  
312 synclines over the rigid hanging wall. In most of our experiments we observe faults that form near the free  
313 surface and propagate downward, evolving through time and space during the different stages of the  
314 experiments, yet they are normally confined at very shallow depth. As already mentioned, these minor faults  
315 are related with the bending moment caused by the upward-propagation of the main newly-formed synthetic  
316 fault. Shallow downward-propagating structures form in five experiments: E1, E2, E3, E6, and E7. They are  
317 located along the anticline axis, i.e. where the tensile stress due to bending is largest. In contrast, downward-  
318 propagating faults do not form at all in E4 and E5, likely because slip on the main synthetic fault reaches the  
319 free surface during the very early stages of deformation (Fig. 10b), thereby minimizing the bending moment  
320 at shallow depth. Hereafter, we adopt the vertical projection to the free surface of the tip of the master fault on  
321 the footwall rigid block as a reference for the position of these shallow faults (Fig. 10c); positive distance is  
322 toward the footwall.

323 At the free surface of the isotropic experiment (E1) the first structure nucleates near the anticline axis at a  
324 distance of 2.0 cm (Figs. 3, and 10c). The second surface fault forms at a shorter distance and links with the  
325 upward-propagating fault during the late stage of the experiment.

326 In E2, a shallow brittle structure forms since the Early Stage, likely because the development of the fold related  
327 with the upward-propagating fault is faster than in other experiments. This shallow fault is located farther away  
328 into the footwall than shallow faults observed in other experiments (Fig. 10c), yet it remains within the trishear  
329 zone. In the Middle Stage, other shallow faults quickly form at shorter distance but showing only little offset.

330 In E3 a shallow fault displaces the free surface at 2.5 cm distance in the Middle Stage (Figs. 4, and 10c). During  
331 the Late Stage most of the surface deformation concentrates on this fault because of the significant slowdown  
332 in the evolution of the upward-propagating but still blind faults, likely as a result of the interaction with the  
333 precut. This interaction causes a small change of the monocline shape, and, consequently, the maximum tensile

334 stress is always located in the same portion of the fold. Minor faults located at shorter distance are related to  
335 the progression of the - minimal, yet clearly visible - fold.

336 In E6 (Fig. 8) and E7 (Fig. 9), the downward-propagating faults are well developed and offset significantly the  
337 free surface. This is due to the reactivation of the pre-cut that tightens the anticline at shallow depth, thereby  
338 increasing the tensile stress on the fold extrados.

339 In all experiments, the downward-propagating faults form progressively from the footwall toward the hanging  
340 wall, though their initial position and vertical offset are variable (Fig. 10c). In the experiments where the  
341 upward-propagating faults reach the surface (E1 and E2) the innermost shallow faults form in the early stages  
342 and are then linked to the upward-propagating faults.

#### 343 **4.4. Shape of the free surface and migration of the syncline hinge**

344 The shape of the anticlines and synclines and the position of their hinges control the development of secondary  
345 brittle structures. Such direct correlation was illustrated in Section 4.3 where we highlighted how the shape of  
346 the anticlines and the migration of their hinge points lead to the formation of secondary shallow faults - i.e. the  
347 bending-moment faults - while the master fault remains blind.

348 To analyze the warping of the free surface we construct a formline obtained by connecting the shallowest  
349 displacement vectors; this allows us to avoid including unwanted artifacts due to the unevenness of the top of  
350 the clay layer. All experiments show a different evolution of the fold shape and of the space-time migration of  
351 fold hinges (Fig. 11). To highlight the peculiarities of each experiment, we reconstruct 1) the cumulative and  
352 2) the incremental shape changes (Figs. 11a and 11c, respectively) at the same intervals as in the fault analyses.

353 The cumulative profiles provide a way of comparing our experimental results with the bedrock of a  
354 hypothetical sedimentary basin, i.e. with the shape of the basin floor. Conversely, since erosion, transport, and  
355 deposition processes respond dynamically to the changes of the accommodation space, the incremental profiles  
356 provide useful information on the evolution/architecture of a sedimentary infill. Similarly to the analysis of  
357 shallow faults (Section 4.3), we adopt the vertical projection to the free surface of the tip of the master fault  
358 on the footwall rigid block as a reference for the position of fold axes (Figs. 11b and 11d); in this case, however,  
359 positive distance is toward the hanging wall.

360 A comparison of the hanging wall of all experiments shows anticline limbs with different inclinations and a  
361 variable degree of openness of the synclines (Fig. 11).

362        **4.4.1. Early Stage (from 0 to 0.5 cm)**

363        In the isotropic experiment (E1) the syncline hinge is at about 2.5 cm (Fig. 11a). In most of the other  
364        experiments, the syncline hinge is closer to the tip of the master fault, with the exception of E3 whose syncline  
365        hinge is the farthest (Fig. 11a). Such differences are due to the different propagation rates of the upward-  
366        propagating faults and/or to the amount of slip taken on by the precut. In E3, for instance, the position of the  
367        syncline hinge could be related to the slower development of the upward-propagating fault or to a weak  
368        reactivation of the precut or to both conditions. The syncline hinge of E2 is the closest, likely because of the  
369        faster growth rate of the upward-propagating fault. Regarding E4, E6, and E7, the syncline hinge stays nearly  
370        in the same position even if the fault evolution history and the resulting fold shape are different. Indeed in E4  
371        the reactivation of the synthetic precut produces a very open anticline and syncline, whereas in E6 and E7 slip  
372        on the precut tightens the shape of the syncline without shifting its hinge (Figs. 11a, b). In E7 a small syncline  
373        also forms far away into the hanging wall in correspondence with the precut cutoff and likely due to the partial  
374        reactivation of the precut itself. Notice that in all experiments the subsidence of the syncline hinge is about 0.3  
375        cm (Fig. 11a). In E5 no syncline develops because the early reactivation of the precut quickly transfers slip up  
376        to the free surface, hence drastically shortening the bending phase.

377        **4.4.2. Middle Stage (from 0.5 to 1.0 cm)**

378        In the Middle Stage the differences between subsequent experiments increase, though all syncline hinges  
379        migrate toward the footwall. In E1, the syncline hinge migrates 0.29 cm vertically and 0.6 cm horizontally  
380        (Figs. 11b and 11d). E2, E3, and E4 show a similar trend. Conversely, E6 and E7 display significant lowering  
381        without any horizontal shift. This is likely due to the concurrent evolution of fold-related faulting and slip on  
382        sections of the precut (Figs. 8, 9). This trend is more evident in E6 because the precut is more favorably oriented  
383        for being reactivated (dip=45°). Downward-propagating faults begin to be well developed and offset the free  
384        surface. In E3 the anticline is also reshaped by a small graben-like structure. The precut reactivation in E4  
385        increases the size of the hollow located on the hinge zone of the major anticline. In E2 the fast development of  
386        the upward-propagating fault produces a sort of box fold (Fig. 11a). The analysis of the surface deformation  
387        (Fig. 11c) highlights that this box fold is produced by a rapid migration of the syncline hinge due to the  
388        evolution of the upward-propagating fault. Figures 11b and 11d show that E1, E2, and E3 have approximately

389 the same horizontal shift values, but the vertical component in E1 and E3 is less pronounced than that of E2  
390 and it is insufficient to produce a significant change in the shape of the syncline.

#### 391 **4.4.3. Late Stage (from 1.0 to 1.5 cm)**

392 In E1 the connection between upward- and downward-propagating faults concludes the blind phase of the  
393 system. The synclinal hinge migrates toward the footwall at an almost constant rate (Figs. 11b and 11d). In  
394 E3, the evolution of the upward-propagating fault is drastically slowed down by the precut (Fig. 10b). Such  
395 interaction enhances the little graben near the anticline hinge. In E4 the reactivation of the precut contrasts the  
396 migration of the syncline hinge, resulting in its negligible horizontal shift (Fig. 11d). Figure 11c shows how  
397 the slip on this anti-listric (convex up) fault results in a uniform subsidence of the hanging wall. In E6 and E7  
398 the horizontal migration of the syncline hinge restarts only after that the downward-propagating faults are well  
399 developed and the upward-propagating faults cross the precut.

#### 400 **4.5. Modeling limitations**

401 The geometry and kinematics of faults and folds that develop in an extensional system where variably oriented  
402 pre-existing discontinuities are located above a master normal fault can be successfully simulated using analog  
403 modeling. Before applying our results to analyze natural systems, however, it is important to consider some  
404 intrinsic limitations of our experiments.

405 Our experimental apparatus reproduces a planar, 45°-dipping master fault. In nature, extensional faults may  
406 have a listric geometry that induces hanging wall deformation driven by the sliding of rocks on a curved fault  
407 surface (e.g. rollover and drag folds), potentially broadening the newly-generated accommodation space  
408 (Resor and Pollard, 2012). Friction on the master fault plane and secondary normal- and reverse-drag folds or  
409 a combination thereof may also control hanging wall deformation (e.g., Schlische, 1995).

410 Other important limitations regard the frictional properties and the number of precuts within the clay layer.  
411 They may strongly affect the evolution of the extensional system, amplifying or reducing phenomena that we  
412 observe in our experiments (Roering et al., 1997). The shear strength of the precut also depends on its depth,  
413 because the deeper the precut, the higher the normal stress acting on it. Therefore, for any given precut setting,  
414 a shallower precut can be reactivated more easily. A better characterization of precuts also improves the  
415 possibility of comparing them to natural discontinuities.

416 In nature, the dip of the master fault strongly affects both the associated folds and any secondary brittle  
417 structures (Withjack et al., 1990). When the master fault is steeper the associated fold is tighter and determines  
418 an early development of bending-moment faults. Conversely, when the master fault dip is gentler, the  
419 associated fold is open and the extensional structures – or downward-propagating faults – may not form at all  
420 because the curvature radius is larger. Moreover, the normal faults may rotate during the evolution (domino  
421 rotation), changing their dip and affecting the shape of the accommodation space.

422 The usage of rigid hanging wall and footwall blocks is yet another simplification. In the case of seismogenic  
423 faults, for instance, surface deformation is not only produced by coseismic elastic dislocation but also by  
424 postseismic relaxation. This is related with the viscous roots and the viscoelastic properties of the lower crust  
425 and upper mantle that may contribute to the surface deformation by increasing the wavelength of the surface  
426 displacement (Wang et al., 2006; Bürgmann and Dresen, 2008).

#### 427 **4.6. Natural extensional systems**

428 Several currently active extensional systems are located in continental regions that were affected by  
429 contractional processes in earlier tectonic phases. These tectonic systems may exhibit various degrees of  
430 structural maturity depending on the age of inception and on the strain rate of the ongoing extension.

431 In a very early stage, the extension of an orogenic belt is mainly, though not exclusively, testified by earthquake  
432 focal mechanisms and geodetic strain. For instance, the Pyrenees is a mountain chain where the landscape is  
433 still dominated by geomorphic features generated in a contractional setting, but where the analysis of focal  
434 mechanisms demonstrates that current deformation is dominantly extensional (Chevrot et al., 2011; Lacan and  
435 Ortuño, 2012). Considering the tectonic setting of the region and, specifically, the double vergence of the  
436 chain, one could speculate that in the Pyrenees some interactions between older contractional structures and  
437 younger extensional faults might be occurring in a framework similar to either E4-5 or E6-7.

438 Such interactions have been extensively documented also in the Apennines, where recent earthquakes shed  
439 light on the direct interaction between youthful extensional faults and inherited thrusts that affect both their  
440 development and their surface signature. For example, Miocene thrusts appear to control the extent of 40°-  
441 dipping normal faults that were responsible for the  $M_w$  6.0 and 5.7 mainshocks of the September 1997,  
442 Colfiorito, earthquake sequence (Chiaraluce et al., 2003). In the case of the April 2009, L'Aquila earthquake  
443 sequence the first mainshock (6 April,  $M_w$  6.3) was caused by slip on a 40-50°-dipping normal fault; this master

444 fault branches upward at 3-5 km depth where it intersect a Miocene thrust dipping  $10^\circ$  in the same dip direction  
445 as the master fault and creates bending-moment faulting at the ground surface (Bonini et al., 2014). In the  
446 second mainshock (7 April,  $M_w$  5.4), that was caused by another  $40\text{-}50^\circ$ -dipping normal fault with an upper  
447 limit at about 5 km depth, just below a  $20\text{-}30^\circ$ -dipping Miocene thrust; as a result, it showed no connection  
448 with the normal faults lying above it, especially well imaged by seismic reflection lines (Bigi et al., 2013).  
449 Altogether these examples recalls the early-middle stages of E3 and E4 and, considering cases analyzed by  
450 Valensise and Pantosti (2001), suggest that other large active normal faults in the Apennines may be  
451 developing in a framework similar to any other of our experiments.

452 In summary, although extension is currently the dominating tectonic mechanism both in the Pyrenees and in  
453 the Apennines, the structural architecture of these orogens reflects the activity of the large seismogenic normal  
454 faults only to a very limited extent. Instead, their landscape and their earthquake potential are clearly dominated  
455 by the interaction with inherited contractional structures, which ultimately affect the length, the width and the  
456 top depth of the active normal faults.

457 Another example of such interactions has been documented in the northern part of the Taiwan orogen that is  
458 affected by late Quaternary extension (e.g. Suppe, 1984; Teng, 1996; Hu et al., 2002). An active normal fault  
459 (Shanchiao Fault) located in the Taipei basin shows a ramp-flat-ramp geometry whose deeper ramp (dipping  
460  $60^\circ$ ) is an ancient extensional fault inherited from a pre-contractional phase (rifting phase of the Chinese  
461 Continental Margin). Its flat portion (dipping  $15^\circ$ ) is a Neogene thrust fault, whereas the shallower ramp is a  
462 late Quaternary - hence newly-formed - normal fault (Chen et al., 2014). It is plausible that Quaternary  
463 extension reactivated the ancient extensional fault at depth, which propagated upward exploiting a segment of  
464 the low-angle inherited thrust and then reached the ground surface forming a new high-angle, normal fault.  
465 This unusual case of Quaternary fault development is reminiscent of the results of E3 and E4, and shows that  
466 also a  $60^\circ$ -dipping extensional fault, i.e. a fault steeper than the master faults in our experiments, may stop its  
467 upward propagation against an inherited low-angle structure.

468 Conversely, in a mature system the extensional faults are expected to be well developed and expressed at the  
469 surface. The Basin and Range Province is a renowned example of such a mature extensional system. However,  
470 also in this region extensional structures overprint older contractional structures (e.g. Wernicke, 1992; Parsons,  
471 1995; Axen, 2007). Studies on major earthquakes of this area (e.g. the  $M_w$  7.3, 1959, Hebgen Lake, Montana,

472 and the  $M_w$  6.9, 1983, Borah Peak, Idaho) demonstrate that the normal faults exposed at the surface are the  
473 direct expression of large, planar faults dipping  $40^\circ$  to  $70^\circ$  and extending down to 12-16 km depth (Barrientos  
474 et al., 1987; Doser, 1989). Notice, however, that some of these fault planes coincide at depth with pre-existing  
475 contractional structures (thrust faults) reactivated as normal faults during the extensional phase (Doser, 1989;  
476 West, 1992) in a way very similar to what can be observed in E4 and E5. The existence of youthful faults  
477 confined at depth (blind faults) and interacting with inherited thrusts that are unfavorably oriented with respect  
478 to the current stress field was described in great detail by West (1989; 1992), testifying that inherited structures  
479 may play an active role even in regions that exhibit a hypermature stage of development.

480 In summary, depending on the local configuration or on the degree of structural maturity, the inherited  
481 structures may directly affect the evolution of youthful extensional faults. Our experiments may help  
482 characterizing the evolutionary stage of these faults and understand the causal relationships between the master  
483 fault at depth and other structural and geomorphic features.

484

## 485 **5. Conclusions**

486 We investigated how pre-existing discontinuities affect the growth of extensional structures connected to the  
487 displacement on an initially-blind master normal fault. To this end, we used analog models that take advantage  
488 of an innovative technique for performing a precut into a clay (wet kaolin) layer laid on top of a master fault,  
489 simulated by the sliding of two rigid blocks. Using this original setup, we carried out six experiments in which  
490 the precut has various orientations with respect to the master fault, and compared them to another experiment  
491 without any precut (isotropic). All other conditions were identical for all seven experiments.

492 Our results show that the presence of a precut can either accelerate or decelerate the upward propagation of  
493 the master fault and exert control on several other factors summarized below and in Table 1;

- 494 • a horizontal precut promotes the tendency to grow of upward-propagating faults;
- 495 • low-angle synthetic precuts (e.g. dip  $10^\circ$ ) slow down the propagation of upward-propagating faults,  
496 but also promote the formation and evolution of shallow downward-propagating surface faults  
497 associated with bending moment;

- 498       • high-angle precuts ( $\text{dip} > 30^\circ$ ) are prone to be reactivated and may serve as a preferential way for the  
499           master fault to quickly transfer slip up to the free surface. If the dip of the precut is lower than that of  
500           the master fault, the new fault system will show an antilistric geometry;
- 501       • when the precut is antithetic with respect to the master fault one may expect an increase of the growth  
502           of the upward-propagating faults and a reactivation of the precut as antithetic faults;
- 503       • the various interactions between the growing master fault and the precut also affect the shape of the  
504           fault-related syncline-anticline pair and, in turn, the shape of the resulting accommodation space.

505 These findings may improve our understanding of how extensional fault systems evolve in presence of  
506 structures inherited from previous tectonic phases, such as the normal faults that currently affect older orogenic  
507 belts. We also suggest that the analysis of the shape and architecture of fault-related continental basins carried  
508 out in the light of our findings may provide useful constraints for reconstructing the actual geometry of the  
509 master fault at depth.

510

#### 511 **Acknowledgements**

512 All experiments were carried out at the 3D Modelling Laboratory at University of Pavia  
513 ([www.3dmodellinglaboratory.it](http://www.3dmodellinglaboratory.it)). The work was supported by the INGV Project “Abruzzo” (code:  
514 RBAP10ZC8K\_003), funded by the Italian Ministry for Education, University and Research (MIUR).

515

516

517

518

519

520

521

522

523

524

525

526 **References**

- 527 Ahmad, M.I., Dubey, A.K., Toscani, G., Bonini, L., Seno, S., 2014. Kinematic evolution of thrust wedge and  
528 erratic line length balancing: insights from deformed sandbox models. *International Journal of Earth*  
529 *Sciences*, 103, 1, 329-347, doi:10.1007/s00531-013-0947-8.
- 530 Axen, G., 2007. Research Focus: Significance of large-displacement, low-angle normal faults. *Geology*, 35,  
531 287-288, doi:10.1130/0091-7613(2007)35[287:RFSOLL]2.0.CO;2.
- 532 Allmendinger, R.W., 1998. Inverse and forward numerical modeling of trishear fault-propagation folds.  
533 *Tectonics*, 17, 640-656, doi: 10.1029/98TC01907.
- 534 Barrientos, S.E., Stein, R.S., Ward, S.N., 1987. Comparison of the 1959 Hebgen Lake, Montana and the 1983  
535 Borah Peak, Idaho, earthquakes from geodetic observations. *Bulletin of the Seismological Society of*  
536 *America*, 77, 784-808.
- 537 Bigi, S., Casero, P., Chiarabba, C., Di Bucci, D., 2013. Contrasting surface active faults and deep seismogenic  
538 sources unveiled by the 2009 L'Aquila earthquake sequence (Italy). *Terra Nova*, 25, 21-29.
- 539 Bonini, L., Dallagiovanna, G., Seno, S., 2010. The role of pre-existing faults in the structural evolution of  
540 thrust systems: insights from Ligurian Alps (Italy). *Tectonophysics*, 480, 73-87.  
541 doi: 10.1016/j.tecto.2009.09.021
- 542 Bonini, L., Di Bucci, D., Toscani, G., Seno, S., Valensise, G., 2011. Reconciling deep seismogenic and shallow  
543 active faults through analogue modelling: the case of Messina Straits (southern Italy). *Journal of the*  
544 *Geological Society*, 168 (1), 191-199. doi: 10.1144/0016-76492010-055
- 545 Bonini, L., Di Bucci, D., Toscani, G., Seno, S., Valensise, G., 2014. On the complexity of surface ruptures  
546 during normal faulting earthquakes: excerpts from the 6 April 2009 L'Aquila (central Italy) earthquake  
547 (Mw 6.3). *Solid Earth*, 5, 389-408, doi:10.5194/se-5-389-2014.
- 548 Bürgmann, R., Dresen, G., 2008. Rheology of the lower crust and upper mantle: evidence from rocks  
549 mechanics, geodesy, and field observations. *Annu. Rev. Earth Planet. Sci.*, 36, 531-557,  
550 doi:10.1146/annurev.earth.36.031207.124326.
- 551 Chen, C.-T., Lee, J.-C., Chan, Y.-C., Lu, C.-Y., Teng, L.S.-Y., 2014. Elucidating the geometry of the active  
552 Shanchiao Fault in the Taipei metropolis, northern Taiwan, and the reactivation relationship with pre-  
553 existing orogen structures. *Tectonics*, doi: 10.1002/2013TC003502.
- 554 Chevrot, S., Sylvander, M., Delouis, B., 2011. A preliminary catalog of moment tensors for the Pyrenees.  
555 *Tectonophysics*, 510, 239-251.
- 556 Chiaraluca, L., Ellsworth, W.L., Chiarabba, C., Cocco, M., 2003. Imaging the complexity of an active normal  
557 fault system: The 1997 Colfiorito (central Italy) case study. *J. Geophys. Res.*, 108, B6, 2294,  
558 10.1029/2002JB002166.
- 559 Collettini, C., Sibson, R.H., 2001. Normal faults, normal friction? *Geology*, 29(10), 927-930, doi:  
560 10.1130/0091-7613.

561 Cooke, M.L., Mollema, P., Pollard, D.D., Aydin, A., 2000. Interlayer slip and fracture clusters within East  
562 Kaibab monocline: numerical analysis and field investigations. Geological Society of London Special  
563 Publication - Drape folds and Associated Fractures, eds. J. Cosgrove, M. Ameen. 169, 23-49.

564 Cooke, M.L., Madden, H.M., 2014. Is the Earth Lazy? A review of work minimization in fault evolution.  
565 Journal of Structural Geology, 66, 334-346.

566 Cooke, M.L., Schottenfeld, M.T., Buchanan, S.W., 2013. Evolution of fault efficiency at restraining bends  
567 within wet kaolin analog experiments. Journal of Structural Geology, 51, 180-192.

568 Cooke, M.L., Pollard, D.D., 1997. Bedding-plane slip in initial stages of fault-related folding. Journal of  
569 Structural Geology, 19, 3, 567-581.

570 Cooke, M.L., van der Elst, N.J., 2012. Rheologic testing of wet kaolin reveals frictional and bi-viscous  
571 behavior typical of crustal materials. Geophysical Research Letters, 39,  
572 <http://dx.doi.org/10.1029/2011GL050186>.

573 Cosgrove, J.W, Ameen, M.S., 2000. A comparison of the geometry, spatial organization and fracture patterns  
574 associated with forced folds and buckle folds. Geological Society of London Special Publication -  
575 Drape folds and Associated Fractures, eds. J. Cosgrove, M. Ameen. 169, 7-21.

576 d'Alessio, M.A., Martel, S.J., 2004. Fault terminations and barriers to the fault growth. Journal of Structural  
577 Geology, 26, 1885-1896.

578 Dalmayrac, B., Molnar, P., 1981. Parallel thrust and normal faulting in Peru and constraints on the state of  
579 stress. Earth Planet. Sci. Lett., 55, 473-481.

580 Davis, D., Suppe, J., Dahlen, F.A., 1983. Mechanics of fold-and-thrust belts and accretionary wedges. Journal  
581 of Geophysical Research, 88 (B2), 1153-1172.

582 Doser, D.I., 1989. Source parameters of Montana earthquakes (1925-1964) and tectonic deformation in the  
583 northern Intermountain Seismic Belt. Bulletin of the Seismological Society of America, 79, 31-50.

584 Eisenstadt, G., Sims, D., 2005. Evaluating sand and clay models; do rheological differences matter? Journal  
585 of Structural Geology, 27, 1399-1412, 2005.

586 Elter, P., Giglia, G., Tongiorgi, M., Trevisan, L., 1975. Tensional and compressional areas in the recent  
587 (Tortonian to present) evolution of the Northern Apennines. Boll. Geofis. Teor. Appl., 42, 3-18.

588 Faccenna, C., Nalpas, T., Brun, J.P., Davy, P., Bosi, V., 1995. The influence of pre-existing faults on normal  
589 fault geometry in nature and in experiments. Journal of Structural Geology, 17, 1139-1149.

590 Galuppo, C., Toscani, G., Turrini, C., Bonini, L., Seno, S., 2015. Fracture patterns evolution in sandbox fault-  
591 related anticlines. Italian Journal of Geosciences, doi: 10.3301/IJG.2014.39.

592 Garcia, D., 2011. A fast all-in-one method for automated post-processing of PIV data. Experiments in Fluids,  
593 Springer-Verlag, 2011, 50, 1247-1259.

594 Gudmundsson, A., 2011. Rock fractures in geological processes. Cambridge University Press.

595 Hardy, S., Ford, M., 1997. Numerical modelling of trishear fault-propagation folding and associated growth  
596 strata. Tectonics, v. 16, no. 5, p. 841-854.

597 Hu, J.-C., Yu, S.-B., Chu, H.-T., Angelier, J., 2002. Transition tectonics of northern Taiwan induced by  
598 convergence and trench retreat. *Geological Society of America Special Paper*, 358, 149-162.

599 Hubbert, M.K., 1937. Theory of scale models as applied to the study of geologic structures. *Geological Society*  
600 *of America Bulletin*, 48, 1459–1520.

601 Hutchinson, J.W., 1996. Stresses and failure modes in thin films and multilayers. Notes for a DCAMM Course.  
602 Lyngby: Technical University of Denmark, pp. 1-45.

603 Hyppolite, J.-C., Angelier, J., Roure, F., 1994. A major geodynamic change revealed by Quaternary stress  
604 patterns in the Southern Apennines (Italy). *Tectonophysics*, 230, 199–210.

605 Jackson, J.A., White, N.J., 1989. Normal faulting in upper continental crust: observations from regions of  
606 active extension. *Journal of Structural Geology*, 11, 15-36.

607 Lacan, P., Ortuño, M., 2012. Active Tectonics of the Pyrenees: A review. *Journal of Iberian Geology*, 38 (1)  
608 2012: 9-30.

609 Maino, M., Decarlis, A., Felletti, F., Seno, S., 2013. Tectono-sedimentary evolution of the Tertiary Piedmont  
610 Basin (NW Italy) within the Oligo-Miocene central Mediterranean geodynamics. *Tectonics*, 32 (3),  
611 593-619. DOI: 10.1002/tect.20047

612 Malavieille, J., 1993. Late orogenic extension in mountain belts: insights from the Basin and Range and the  
613 Late Paleozoic Variscan Belt. *Tectonics*, 12, 5, 1115-1130.

614 Mandl, G. 2000. *Faulting in brittle rocks: an introduction to the mechanics of tectonic faults*. Springer-Verlag  
615 Berlin Heidelberg New York.

616 Martel, S.J., Pollard, D.D., Segall, P., 1988. Development of simple fault zones in granitic rock, Mount Abbot  
617 quadrangle, Sierra Nevada, California. *Geological Society of America Bulletin*, 100, 1451–1465.

618 Miller, J.F., Mitra, S., 2011. Deformation and secondary faulting associated with basement-involved  
619 compressional and extensional structures. *AAPG Bulletin*, 95, 4, 675-689.

620 Molnar, P., England, P., Martinod, J., 1993. Mantle dynamics, uplift of the Tibetan plateau, and the Indian  
621 monsoon. *Rev. Geophys.*, 31, 357-396.

622 Pan, B., Qian, K., Xie, H., Asundi, A., 2009. Two-dimensional digital image correlation for in-plane  
623 displacement and strain measurement: a review. *Meas. Sci. Technol.*, 20, doi:10.1088/0957-  
624 0233/20/6/062001.

625 Parsons, T., 1995. The Basin and Range Province, in *Continental Rifts: Evolution, Structure and Tectonics*,  
626 Olsen, K., ed., Amsterdam, Elsevier, ISBN 044489-566-3, p. 277-324. Accessed 25 September 2014  
627 from United States Geological Survey web site.  
628 [https://profile.usgs.gov/myscience/upload\\_folder/ci2012Jun2518224342680BRP\\_review\\_opt.pdf](https://profile.usgs.gov/myscience/upload_folder/ci2012Jun2518224342680BRP_review_opt.pdf)

629 Paul, D., Mitra, S., 2013. Experimental models of transfer zones in rift systems. *AAPG Bulletin*, 97, 5, 759-  
630 780.

631 Philippon, M., Willinghofer, E., Sokoutis, D., Corti, G., Sani, F., Bonini, M., Cloetingh, S., 2015. Slip re-  
632 orientation in oblique rifts. *Geology*, 43, 147-150.

633 Pollard, D., A. Aydin, 1988. Progress in understanding jointing over the past century. *Geological Society of*  
634 *America Bulletin*, v. 100, 1181-1204.

635 Resor, P.G., Pollard, D.D., 2012. Reverse drag revisited: Why footwall deformation may be the key to inferring  
636 listric fault geometry. *Journal of Structural Geology*, 41, 98-109.

637 Roche, V., Homberg, C., Rocher, M., 2013. Fault nucleation, restriction, and aspect ratio in layered sections:  
638 Quantification of the strength and stiffness roles using numerical modeling. *Journal of Geophysical*  
639 *Research*, 188, 4446-4460, doi:10.1002/jgrb.50279, 2013.

640 Roering, J.J., Cooke, M.L., Pollard, D.D., 1997. Why blind thrust faults do not propagate to the Earth's surface:  
641 numerical modeling of coseismic deformation associated with thrust-related anticlines. *Journal of*  
642 *Structural Geology*, 102, 901-912.

643 Schlische, R., 1995. Geometry and origin of fault-related folds in extensional settings. *AAPG Bulletin*, 79, 11,  
644 1661-1678.

645 Scholz, C.H., 2002. *The Mechanics of Earthquakes and Faulting*. 2nd ed., 471 pp., Cambridge University  
646 Press, New York.

647 Segall, P., Pollard, D.D., 1983. Nucleation and growth of strike slip faults in granite. *Journal of Geophysical*  
648 *Research*, 88, 555-568.

649 Selverstone, J., 1988. Evidence for east-west crustal extension in the Eastern Alps: implications for the  
650 unroofing history of the Tauern Window. *Tectonics*, 7, 87-105.

651 Suppe, J., 1984. Kinematics of arc-continent collision, flipping of subduction and back-arc spreading near  
652 Taiwan. *Memoir of the Geological Society of China*, 6, 21-33.

653 Tavarnelli, E., 1996a. Ancient synsedimentary structural control on thrust ramp development: examples from  
654 the Northern Apennines, Italy. *Terra Nova*, 8, 65-74.

655 Tavarnelli, E., 1996b. The effects of pre-existing normal faults on thrust ramp development: an example from  
656 the Northern Apennines, Italy. *International Journal of Earth Sciences*, 85, 363-371.

657 Tavarnelli E., Decandia, F.A., Renda, P., Tramutoli, M., Gueguen E., Alberti M., 2001. Repeated reactivation  
658 in the Apennine-Maghrebide system, Italy: a possible example of fault-zone weakening? *Geological*  
659 *Society of London Special Publication* 186, "The Nature and Tectonic Significance of Fault Zone  
660 Weakening" (Holdsworth, R.E., Strachan, R.A., Magloughlin, J.F. & Knipe, R.J. , Eds.), 273-286.

661 Tavarnelli E., Renda, P., Pasqui, V., Tramutoli, M., 2003. The effects of post-orogenic extension on different  
662 scales: an example from the Apennine-Maghrebide fold-and-thrust belt, SW Sicily. *Terra Nova*, 15, 1-  
663 7

664 Teng, L.S., 1996. Extensional collapse of the northern Taiwan mountain belt. *Geology*, 24, 10, 949-952.

665 Thielicke, W., 2014. *The Flapping Flight of Birds - Analysis and Application*. Phd thesis, Rijksuniversiteit  
666 Groningen.

667 Thielicke, W., Stamhuis, E.J., 2014. PIVlab - Time-Resolved Digital Particle Image Velocimetry Tool for  
668 MATLAB version: 1.35. <http://dx.doi.org/10.6084/m9.figshare.1092508>.

669 Tong, H., Koyi, H., Huang, S., Zhao, H., 2014. The effect of multiple pre-existing weaknesses on formation  
670 and evolution of faults in extended sandbox models. *Tectonophysics*, 626, 197-212.

671 Toscani, G., Bonini, L., Ahmad, M.I., Di Bucci, D., Di Giulio, A., Seno, S., Galuppo, C., 2014. Opposite  
672 verging chians sharing the same foreland: kinematics and interaction through analogue models  
673 (Central Po Plain, Italy). *Tectonophysics*, 633, 268-282. doi: 10.1016/j.tecto.2014.07.019

674 Tvedt, A.B.M., Rotevatn, A., Jackson, A.-L., Fossen, H., Gawthorp, R.L., 2013. Growth of normal faults in  
675 multilayer sequences: A 3D seismic case study from the Egersund Basin, Norwegian North Sea.  
676 *Journal of Structural Geology*, 55, 1-20.

677 Valensise, G., Pantosti, D., 2001. The investigation of potential earthquake sources in peninsular Italy: a  
678 review. *Journal of Seismology*, 5, 287-306.

679 van Gent, H.W., Holland, M., Urai, J.L., Loosveld, R., 2010. Evolution of fault zones in carbonates with  
680 mechanical stratigraphy – Insights from scale models using layered cohesive powder. *Journal of*  
681 *Structural Geology*, 32, 1375–1391.

682 Wang, P., Xu, L.R., 2006. Dynamic interfacial debonding initiation induced by incident crack. *International*  
683 *Journal of Solids and Structures*, 43, 6535-6550.

684 Wang, R., Lorenzo-Martín, F., Roth, F., 2006. PSGRN/PSCMP-a new code for calculating co- and post-  
685 seismic deformation, geoid and gravity changes based on the viscoelastic-gravitational dislocation  
686 theory. *Comput. Geosci.*, 32, 527-541, doi: 10.1016/j.cageo.2005.08.006.

687 Williams, G.D., Powell, C.M., Cooper, M.A., 1989. Geometry and kinematics of inversion tectonics. In:  
688 *Inversion Tectonics* (edited by Cooper, M. A. & Williams, G. D.). *Spec. Publ. geol. Soc.* 44,3-15.

689 Wernicke, B., 1981. Low-angle normal faults in the Basin and range province: nappe tectonics in an extending  
690 orogen. *Nature*, 291, 645-648.

691 Wernicke, B., 1992. Cenozoic extensional tectonics of the U. S. Cordillera. In: B. C. Burchfiel, P. W. Lipman,  
692 and M. L. Zoback (Editors), *The Cordilleran Orogen; conterminous U. S. The Geology of North*  
693 *America Volume G-3*, *Geol. Soc. Am.*, Boulder, CO, pp. 553-581.

694 West, M.W., 1992. An integrated model for seismogenesis in the Intermountain Seismic Belt. *Bulletin of the*  
695 *Seismological Society of America*, 82, 3, 1350-1372.

696 West, M.W., 1989. Neotectonics of the Darby-Hogsback and Absaroka thrust plates, Uinta County, Wyoming  
697 and Summit County, Utah with applications to earthquake hazard assessment, Ph.D. Thesis, Colorado  
698 School of Mines, Golden, CO.

699 Withjack, M.O., Callaway, S., 2000. Active normal faulting beneath a salt layer: An experimental study of  
700 deformation patterns in the cover sequence. *AAPG Bulletin*, 84, 5, 627-651.

701 Withjack, M.O., Jamison, W.R., 1986. Deformation produced by oblique rifting. *Tectonophysics*, 126, 99-124.  
702

703 Withjack, M.O., Oloson, J., Peterson, E., 1990. Experimental models of extensional forced folds. *AAPG*  
704 *Bulletin*, 74, 1038-1054.

705 Xu, L.R., Huang, Y.Y., Rosakis, A.J., 2003. Dynamic crack detection and penetration at interfaces in  
706 homogeneous materials: experimental studies and model predictions. *Journal of the Mechanics and*  
707 *Physics of Solids*, 51, 461 – 486.  
708

709 **Table 1** – Summary of initial conditions and results of each experiment.

Initial conditions				Results					
Precut	Dip angle	Dip direction	Propagation rate <sup>1</sup>			Antithetic faults created	Shallow brittle structures created	Syncline hinge migration rate <sup>1</sup>	
			Below precut	Across precut	Above precut				
E1	No	---	---	---	---	Yes	Yes	---	
E2	Yes	Horizontal	---	≈	>	>>	No	Yes	≈
E3	Yes	10°	Synthetic	≈	>	<<	Yes	Yes	≈
E4	Yes	30°	Synthetic	≈	R	R	Yes	No	<
E5	Yes	45°	Synthetic	≈	R	R	Yes	No	---
E6	Yes	45°	Antithetic	≈	>	<	Yes	Yes	<
E7	Yes	30°	Antithetic	≈	>	<	Yes	Yes	<<

710 1) Mathematical symbols represent relative values of propagation and syncline hinge migration rates  
711 with respect to the isotropic experiment (E1); letter “R” stands for precut reactivation.

712

713 **Figure captions**

714

715 **Figure 1.** Schematic cross section showing the early blind phase of an extensional system where new faults  
716 grow up and interact with inherited mechanical discontinuities such as thrust faults.

717 **Figure 2. a)** Plan and side views of the apparatus and initial setup of the isotropic experiment E1. **b-g)** Initial  
718 setups for the precut experiments E2-E7 (the precut is shown by a black, thick line on the side of the clay  
719 layer).

720 **Figure 3.** Side view of the isotropic experiment E1 after 0.5, 1.0 and 1.5 cm of displacement on the master  
721 fault (end of early, middle, and late stages, respectively). The fault traces in the left-hand panels (**a, d, g**) were  
722 detected through visual inspection: the red lines marks the newly-formed faults developed in the specified  
723 stage; black lines are faults formed during previous stages. Central panels (**b, e, h**) show the displacement field  
724 detected using D.I.C. (red arrows) and the boundaries of the trishear zone (dotted lines), when present. Right-  
725 hand panels (**c, f, i**) display the strain-rate distribution.

726 **Figure 4.** Side view of E2 (horizontal precut). The dashed lines mark the precut; other symbols as in Fig. 3.

727 **Figure 5.** Side view of E3 (synthetic, 10° dipping precut). The dashed lines mark the precut; other symbols as  
728 in Fig. 3.

729 **Figure 6.** Side view of E4 (synthetic, 30° dipping precut). The dashed lines mark the precut; other symbols as  
730 in Fig. 3.

731 **Figure 7.** Side view of E5 (synthetic, 45° dipping precut). The dashed lines mark the precut; other symbols as  
732 in Fig. 3.

733 **Figure 8.** Side view of E6 (antithetic, 45° dipping precut). The dashed lines mark the precut; other symbols as  
734 in Fig. 3.

735 **Figure 9.** Side view of E7 (antithetic, 30° dipping precut). The dashed lines mark the precut; other symbols as  
736 in Fig. 3.

737 **Figure 10. a)** Progression of upward propagation of newly-formed fault in the isotropic experiment; the color  
738 shaded area marks the various stages of propagation. **b)** Progression of upward propagation of newly-formed  
739 faults in all experiments. Point symbols mark the position of the precut. Notice that the lines describing the  
740 progression of E4 and E5 become vertical when the newly-formed faults join the pre-existing discontinuity  
741 and reactivate it (Discontinuity Reactivated; D.R.). The orange shaded area marks the zone of the clay layer  
742 where downward-propagating faults tend to develop. **c)** Position of the surface traces of downward-  
743 propagating faults in each experiment. E4 and E5 are not reported because no surficial faults were detected in  
744 these experiments.

745 **Figure 11.** Profiles of the cumulative **(a)** and incremental **(c)** surface deformation of all experiments, except  
746 for E5, after 0.5, 1.0 and 1,5 cm of total displacement on the master fault, and diagrams of the corresponding  
747 cumulative **(b)** and incremental **(d)** migration paths of the synclinal hinges. In all diagrams the point symbols  
748 mark the position of synclinal hinges taken as the lowest point on the profiles.

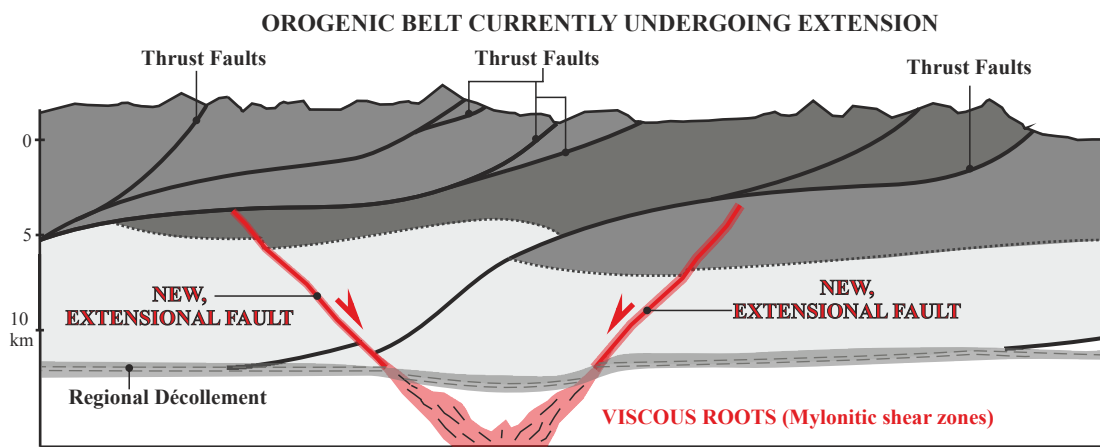


Figure 1

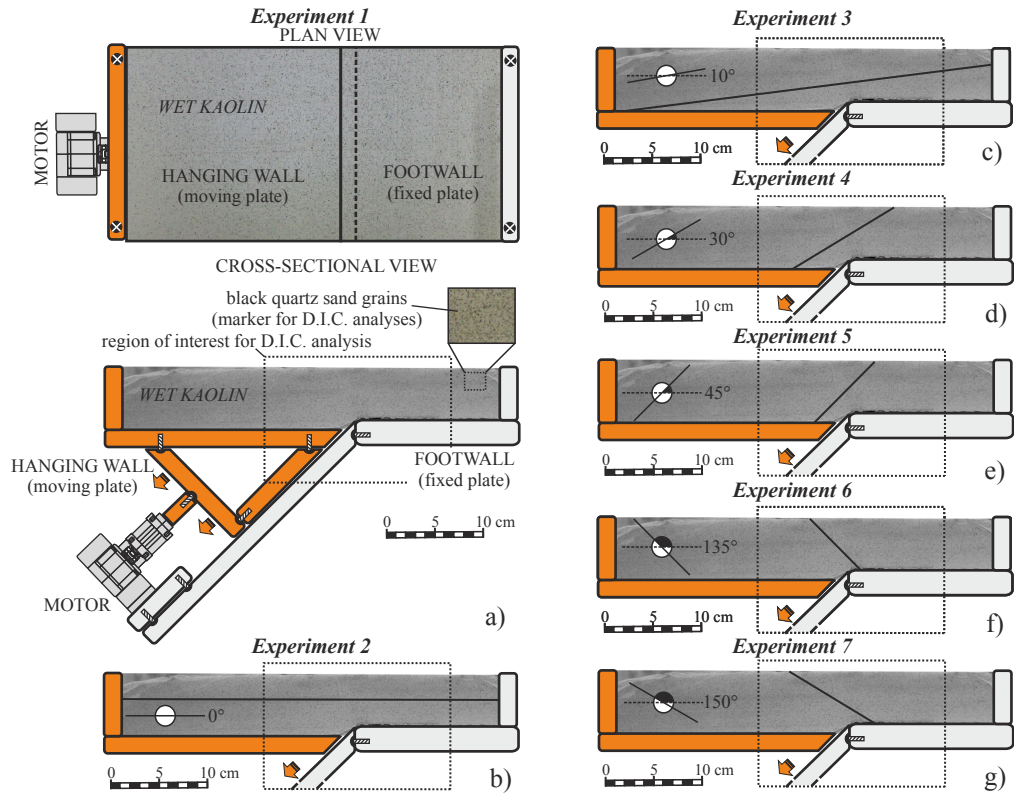


Figure 2

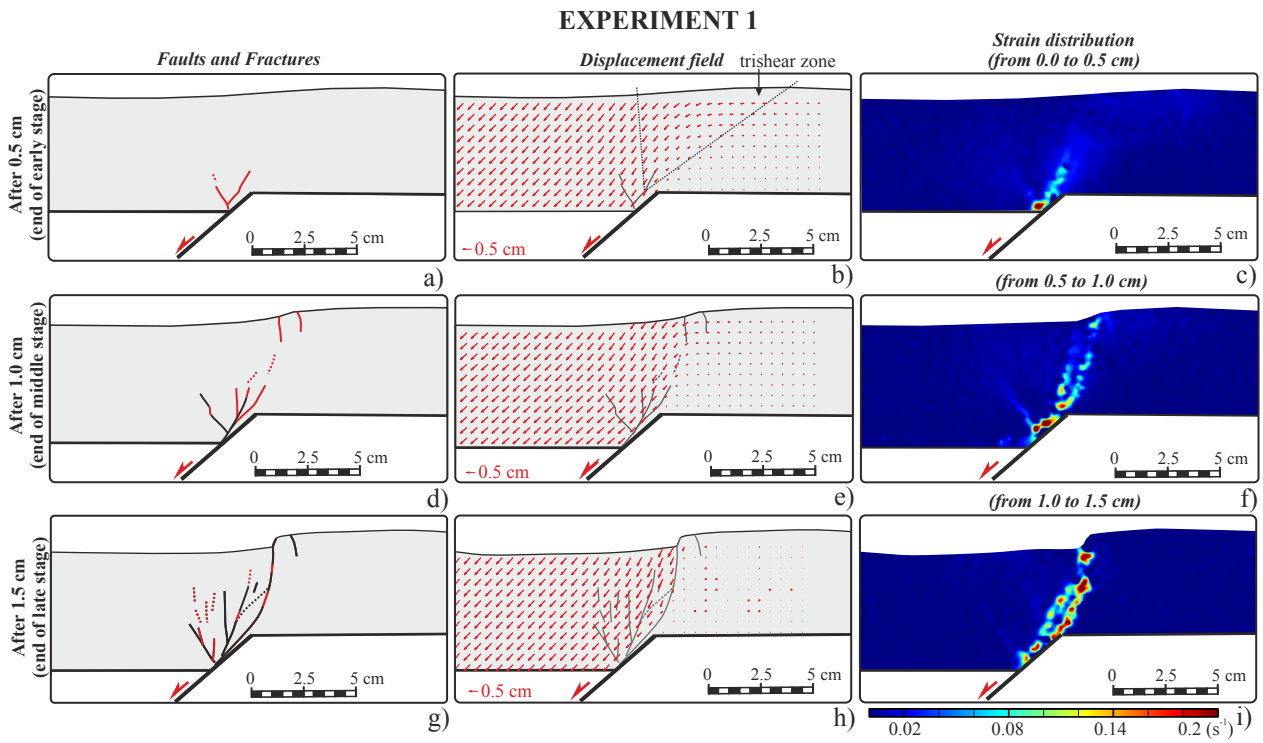


Figure 3

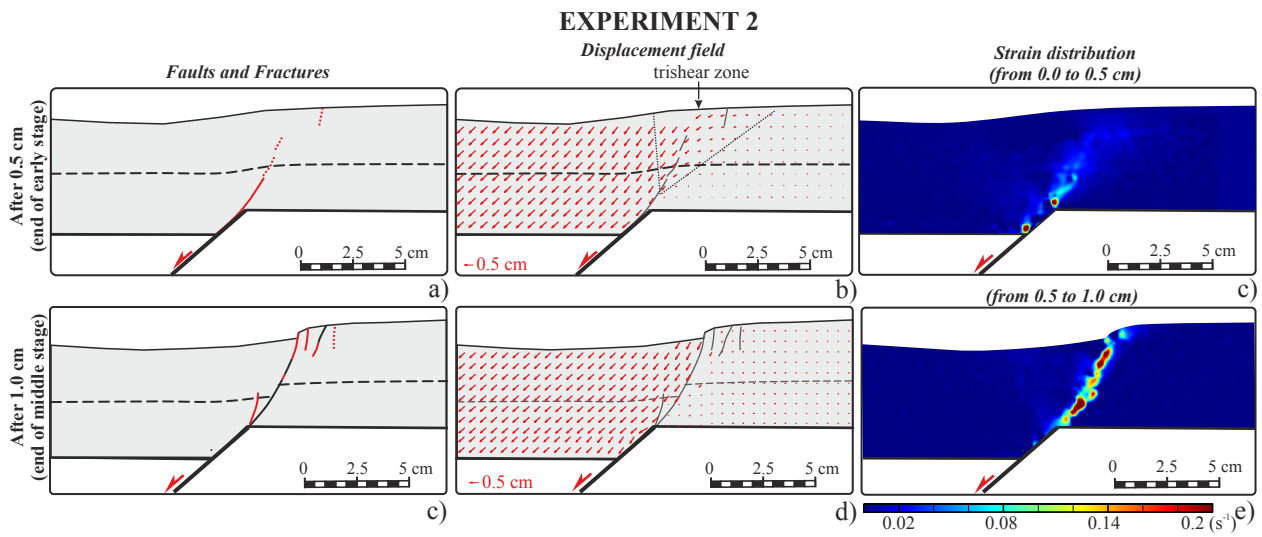


Figure 4

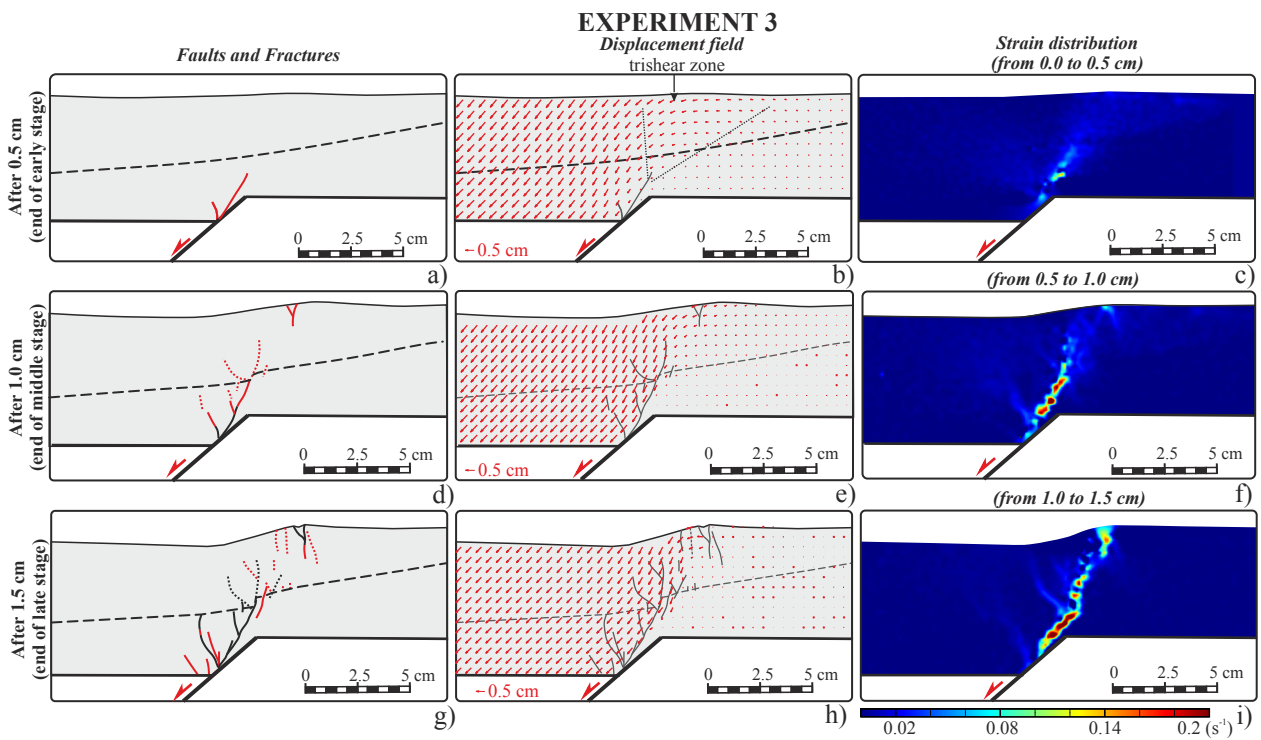


Figure 5

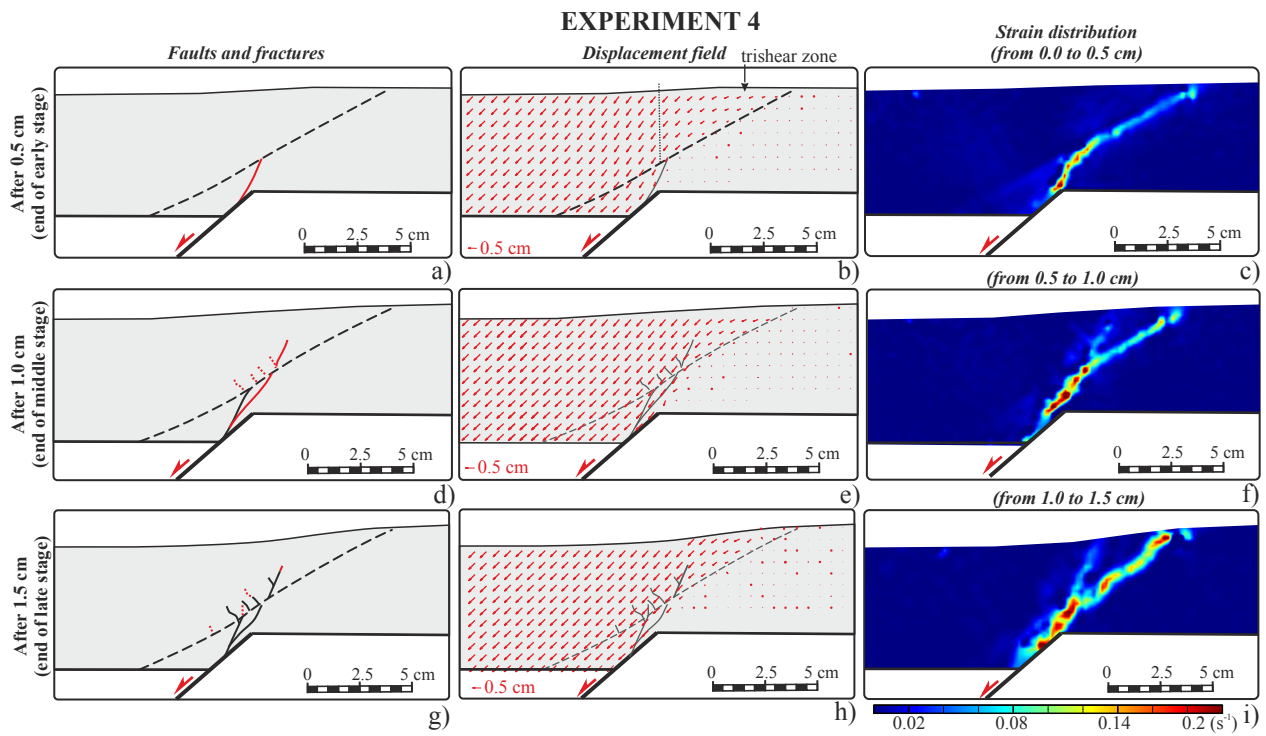


Figure 6

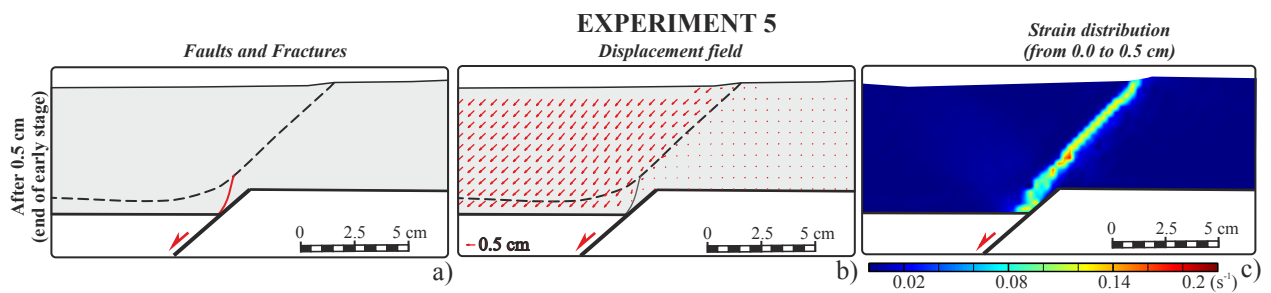


Figure 7

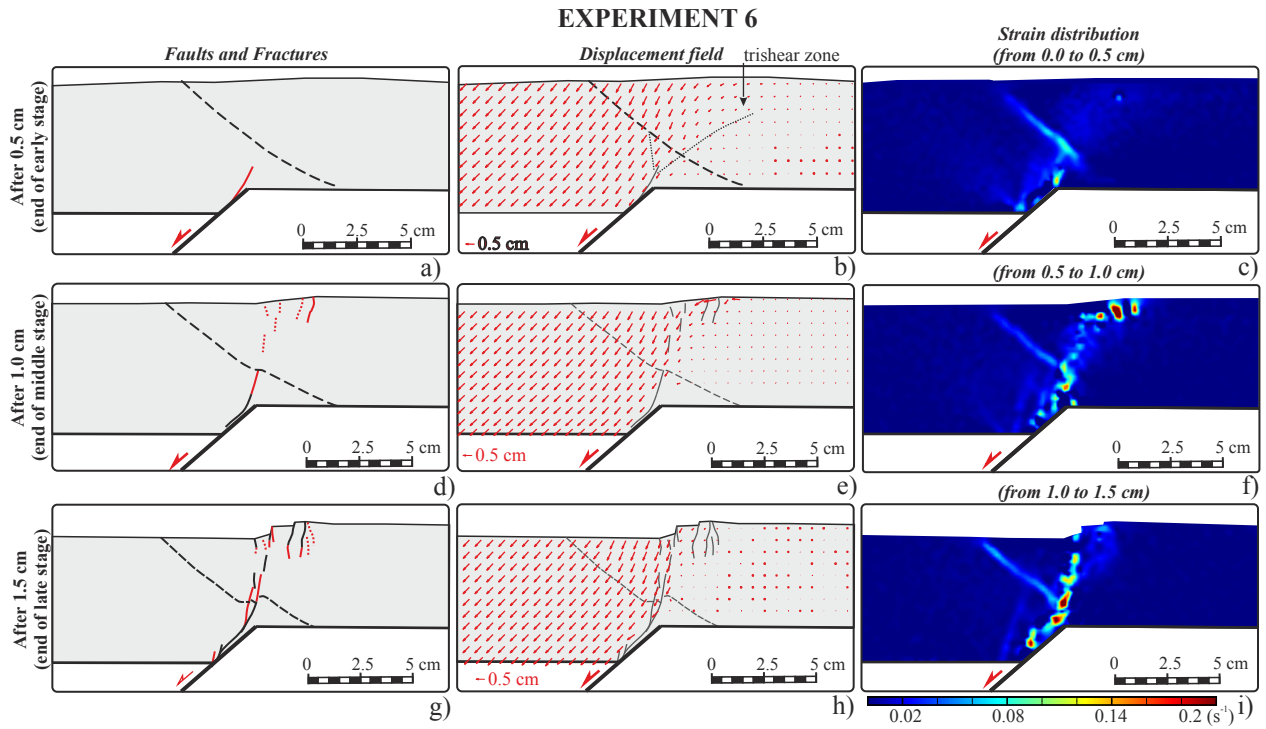


Figure 8

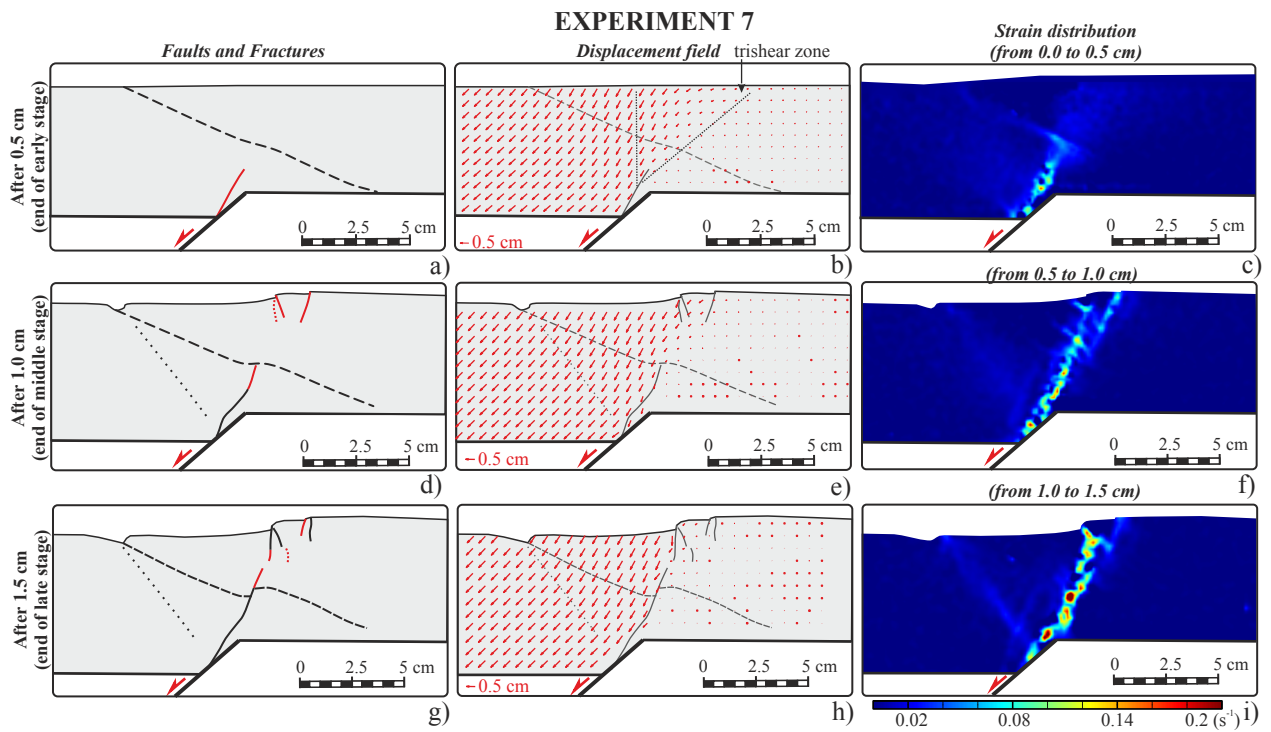
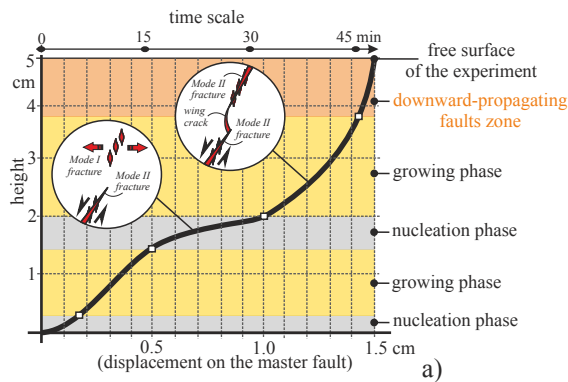
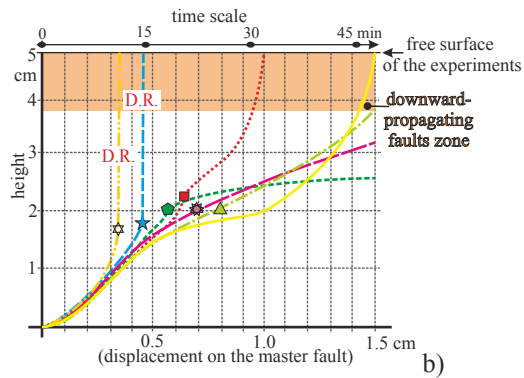


Figure 9

**Upward-propagating faults (height above master fault)  
Isotropic experiment (E1)**



**Upward-propagating faults (height above master fault)**



**Downward-propagating faults (surface traces)**

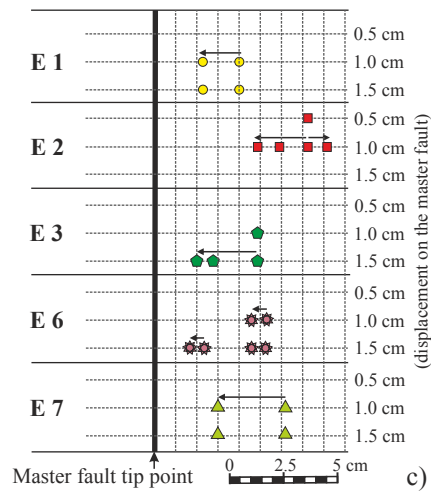


**Figure 10**

